Numerical Simulations of Perforated Plate Liners: Analysis of the Visco-Thermal Dissipation Mechanisms

Robin Billard, Gilles Tissot, Gwenael Gabard, Marc Versaevel

Numerical Simulations of Perforated Plate Liners:

Analysis of the Visco-Thermal Dissipation Mechanisms

R. Billard,[1, a)] G. Tissot,[2] G. Gabard,[1] and Marc Versaevel[3]

[1)] *Laboratoire d'Acoustique de l'Université du Mans, LAUM – UMR CNRS 6613, av. Olivier Messiaen, 72085 Le Mans, France*

[2)] *INRIA Rennes Bretagne Atlantique, IRMAR – UMR CNRS 6625, av. Général Leclerc, 35042 Rennes, France*

[3)] *Safran Nacelles, Route du Pont VIII, 76700 Gonfreville-l'Orcher, France*

(Dated: 18 December 2020)

In the linear regime and in the absence of mean flow, the impedance of perforated liners is driven by visco-thermal effects. In this paper, two numerical models are employed for predicting these visco-thermal losses. The first model is the linearized compressible Navier–Stokes equations (LNSE) solved in the frequency domain. The second model is the Helmholtz equation with a visco-thermal boundary condition accounting for the influence of the acoustic boundary layers. These models are compared and validated against measurements. The quantitative analysis of the dissipation rate due to viscosity, computed from the LNSE solutions of 4 perforated plates, highlights significant differences between the edge effects of a macro- and a micro-perforated plate. In the latter case, a jet is present at the entrances of the perforation. In contrast, the proposed numerical method to calculate the impedance of perforated liners, based on the Helmholtz equation and a visco-thermal boundary condition, is found to be computationally cheaper and to provide reliable predictions.

[a)]robin.billard.etu@univ-lemans.fr; Also at: Safran Nacelles, Route du Pont VIII, 76700 Gonfreville-l'Orcher, France.

I. INTRODUCTION

Perforated plate liners are widely used to reduce noise emissions from turbofans. These liners are the source of aerodynamic losses due to their surface roughness. Such friction losses can be minimized by reducing the surface roughness of the liners, which, as shown experimentally by Roberts (1977), is a function of the plate porosity and the holes diameter. Therefore, using micro perforated plates (MPP), with a porosity σ below 5 % and a neck radius R_{neck} below 0.5 mm, has become of interest to lower the flow drag of the liners.

In the linear regime without mean flow, the main dissipation mechanisms responsible for the acoustic dissipation are the visco-thermal losses. Various models have been proposed for this impedance, such as those of Guess (1975) and Maa (1998) models. In addition, mathematical foundations is proposed by Laurens *et al.* (2013) for the Rayleigh conductivity of cylindrical perforation and unconventional apertures. In a similar modeling effort, Honzk *et al.* (2013) propose a transfer function derived from Zwikker and Kosten (1949) theory to model the viscous and thermal boundary layers in small horns. Joly *et al.* (2006) introduced a formulation of two coupled equations accounting for viscous and thermal effects in a fluid. This formulation is shown to be efficient in solving linear acoustics problems using standard numerical methods.

In the present study, two numerical models are presented and validated, with a view to investigate the acoustic losses occurring at a perforation. The first model solves the Helmholtz equation with a boundary condition accounting for the viscous and thermal acoustics boundary layers from Berggren *et al.* (2018). This boundary condition is obtained by assuming

that the rigid wall is smooth and that its radius of curvature is much greater than the viscous and thermal boundary layers thicknesses. This so-called "Helmholtz with losses" model is compared against a more detailed, but more costly, alternative model based on the linearized compressible Navier–Stokes equations (LNSE). Both models are solved in the frequency domain using finite elements. Their results are compared with impedance tube measurements. This allows to assess the validity of the Helmholtz with losses model. Additionally, the LNSE model allows for a detailed investigation of the losses phenomenon of the micro perforated and the standard macro perforated liners ($\sigma > 5\,\%$, $R_{\text{neck}} > 0.5\,\text{mm}$, defined in section II). The dissipation rate per unit mass due to viscous effects is computed and the difference between micro- and macro-perforate liners are investigated.

The remainder of this paper is as follows. We first present the theoretical models in section II. In section III, a brief description of the numerical methods is given. A comparison between the numerical models and measurements follows in section IV and the dissipation rate is analyzed in section V. In section VI, the convergence of the numerical models is assessed. Finally, we conclude on the relevance of the Helmholtz with losses model in section VII.

II. NUMERICAL MODELS

In this section, two numerical models are described to predict the acoustic impedance of a perforated plate.

The geometry of the perforated plate, which is composed of a periodic arrangement of cylindrical holes is simplified to a single hole. The computational domain is composed of

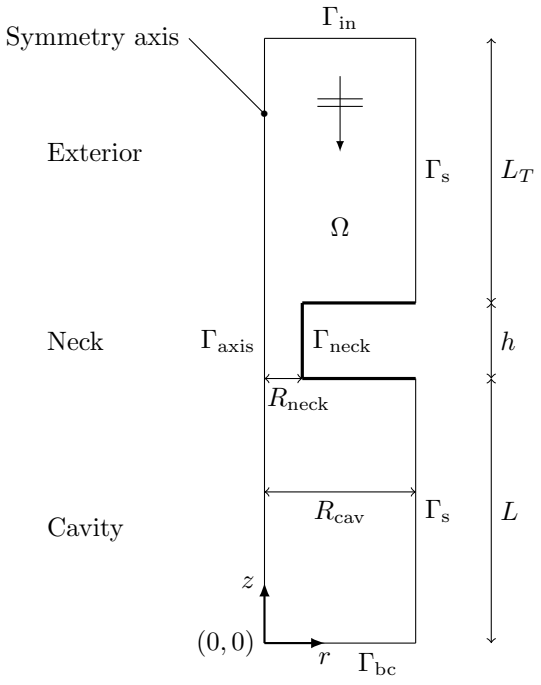

FIG. 1. Axi-symmetric representation of the model.

three cylindrical ducts corresponding to the exterior, the neck and the cavity of the liner. The geometry is further simplified to the 2D axi-symmetrical domain Ω showed in Figure 1.

To ensure that this non-pavable single-hole model is representative of a periodic arrangement of perforations, the Percentage Open Area (POA), also known as porosity σ, must correspond to that of the actual perforated plate. The cavity radius R_{cav}, which is equal to the exterior radius, is chosen to achieve the target plate porosity σ such that

$$\sigma = \left(\frac{R_{\text{neck}}}{R_{\text{cav}}} \right)^2 \tag{1}$$

where R_{neck} is the radius of the neck.

On Figure 1, the Γ_{s} boundary corresponds to sliding surfaces whereas Γ_{bc} and Γ_{neck} are no-slip walls. Γ_{axis} is the symmetry axis of domain Ω. An implicit time dependence $\mathrm{e}^{+\mathrm{i}\omega t}$ is used, where ω is the angular frequency. An incoming plane wave is imposed as a boundary

condition on Γ_{in}. The LNSE and the Helmholtz equation are solved in the domain Ω to calculate the reflected waves and, hence, the reflection coefficient and the effective impedance of the liner.

A. Linearised Navier–Stokes equations

The problem is made non-dimensional by using the following quantities: the sound speed c_0^*, the fluid density ρ_0^* and the reference length $L_{\text{ref}}^* = R_{\text{neck}}$ (recall that $R_{\text{cav}} = R_{\text{neck}}/\sqrt{\sigma}$). The symbol * denotes dimensional quantities. It follows that variables are made non-dimensional as follows

$$x = \frac{x^*}{L_{\text{ref}}^*}\,, \quad \boldsymbol{u} = \frac{\boldsymbol{u}^*}{c_0^*}\,, \quad \rho = \frac{\rho^*}{\rho_0^*}\,, \quad p = \frac{p^*}{\rho_0^* c_0^{*2}}\,, \quad T = \frac{T^* c_p^*}{c_0^{*2}}\,, \quad e = \frac{e^*}{c_0^{*2}}\,.$$

$\boldsymbol{u} = (u_r, u_z)^{\mathrm{T}}$ is the fluid velocity, c is the sound speed, ρ is the density, p is the pressure, T is the temperature, c_p^* is the specific heat capacity at constant pressure and e the specific internal energy.

The acoustic Reynolds number based on the sound speed, and the Prandlt number are defined as follows

$$Re_a = \frac{\rho_0^* c_0^* L_{\text{ref}}^*}{\mu^*} \quad \text{and} \quad Pr = \frac{c_p^* \mu^*}{\kappa^*} \tag{2}$$

where μ^* is the dynamic viscosity and κ^* is the thermal conductivity. Both are assumed independent of temperature.

A perfect gas is assumed, which leads to the following relations between thermodynamic quantities:

$$c^2 = \gamma r T,\ e = \frac{T}{\gamma} \text{ and } p = \rho r T \text{ with } r = \frac{\gamma - 1}{\gamma}.$$

$\gamma = c_p^*/c_v^*$ is the heat capacity ratio and c_v^* is the specific heat capacity at constant volume.

The equations stating the conservation of mass, momentum and energy are as follows:

$$\frac{\partial \rho}{\partial t} + \nabla \cdot (\rho \boldsymbol{u}) = 0, \tag{3}$$

$$\rho \frac{\partial \boldsymbol{u}}{\partial t} + \rho \left(\boldsymbol{u} \cdot \nabla\right) \boldsymbol{u} = -\nabla p + \nabla \cdot \boldsymbol{\tau}, \tag{4}$$

$$\frac{\rho}{\gamma}\left(\frac{\partial T}{\partial t} + \boldsymbol{u} \cdot \nabla T\right) = -p \nabla \cdot \boldsymbol{u} + \boldsymbol{\tau} : \nabla \boldsymbol{u} + \frac{1}{Re_a Pr} \nabla^2 T. \tag{5}$$

The viscous stress tensor $\boldsymbol{\tau}$ is given by

$$\boldsymbol{\tau} = \frac{1}{Re_a}\left[\nabla \boldsymbol{u} + (\nabla \boldsymbol{u})^{\mathrm{T}} + \left(\mu_B - \tfrac{2}{3}\right)(\nabla \cdot \boldsymbol{u})\mathbb{I}\right], \tag{6}$$

where $\mathbb{I}$ is the identity matrix and $\mu_B = \mu_B^*/\mu^*$ is the normalized bulk viscosity. We follow the Stokes hypothesis by setting $\mu_B = 2/3$. This choice, which implies that the effect of dilatation on the viscous stress tensor is removed, is discussed in more details by Schlichting (1979).

The mass conservation equation (3), the momentum conservation equation (4) and the energy conservation equation (5) are linearized around a steady state defined by ρ_0, $\boldsymbol{u}_0$, p_0 and T_0:

$$\rho = \rho_0 + \rho' \,, \quad \boldsymbol{u} = \boldsymbol{u}_0 + \boldsymbol{u}' \,, \quad p = p_0 + p' \,, \quad T = T_0 + T' \,,$$

in which ρ' is the perturbed density, $\boldsymbol{u}'$ is the perturbed velocity, p' is the perturbed pressure and T' is the perturbed temperature. We consider a uniform quiescent medium, hence $\boldsymbol{u}_0 = \boldsymbol{0}$, $\rho_0 = 1$, $c_0 = 1$, $p_0 = 1/\gamma$ and $T_0 = 1/(\gamma - 1)$. In addition we solve these equations in the frequency domain with a $\mathrm{e}^{+\mathrm{i}\omega t}$ time dependence. To discuss the results, we introduce

the thickness δ_V^* of the acoustic viscous boundary layer as well as the shear number Sh:

$$\delta_V^* = \sqrt{\frac{2\mu^*}{\rho_0^*\omega}},\ Sh = \frac{R_{\text{neck}}}{\delta_V^*}. \tag{7}$$

Sh relates the viscous boundary layer thickness to the radius of the perforation. It is useful to distinguish between the macro- and micro-perforated regimes and to assess the range of validity of the Helmholtz equation with losses. When Sh is high, the viscous boundary layer thickness is small compared to the perforation radius.

Therefore, the linearized Navier–Stokes equations reduce to

$$\mathrm{i}\omega\rho' + \nabla\cdot\boldsymbol{u}' = 0, \tag{8}$$

$$\mathrm{i}\omega\boldsymbol{u}' = -\nabla p' + \frac{\omega}{2Sh^2}\nabla\cdot\left[\nabla\boldsymbol{u}' + (\nabla\boldsymbol{u}')^{\mathrm{T}}\right], \tag{9}$$

$$\mathrm{i}\omega T' = -\nabla\cdot\boldsymbol{u}' + \frac{\omega\gamma}{2Sh^2Pr}\nabla^2 T'. \tag{10}$$

Equations (8), (9) and (10) are solved together with the following boundary conditions. This set of equation is for instance implemented in Malinen *et al.* (2004) in the FEM software Elmer to model the thermo-viscous effects in acoustics. Other alternatives are proposed in Kampinga and Wijnant (2010) and Kampinga and Wijnant (2011) in which different formulations of the LNSE are implemented in COMSOL (Pryor, 2009). In the present study we rely on the GetFEM library (Renard and Pommier, 2017). An incident plane wave is defined on the upper boundary of the domain Ω:

$$\nabla p'\cdot\boldsymbol{n} + \mathrm{i}kp' = 2\mathrm{i}kW\mathrm{e}^{+\mathrm{i}kL_Z} \text{ on } \Gamma_{\text{in}}, \tag{11}$$

where $L_Z = L + h + L_T$ and W is the amplitude of the incoming plane wave. k is the acoustic wave number accounting for the viscosity of the fluid and neglecting thermal effects

we obtain:

$$k = \omega \left(1 + \mathrm{i}\omega^2 \frac{\mu_B + \frac{4}{3}}{2Sh^2}\right)^{-\frac{1}{2}} \quad . \tag{12}$$

See A for further detail.

On the perforated plate and the back cover, a no-slip condition is implemented together with an isothermal condition:

$$\boldsymbol{u}' = \boldsymbol{0} \ , \quad T' = 0 \text{ on } \Gamma_{\text{neck}} \text{ and } \Gamma_{\text{bc}} \ . \tag{13}$$

Alternatively, we will also consider the case where an adiabatic condition is imposed by setting $\nabla T' \cdot \boldsymbol{n} = 0$ on these surfaces. In section IV, we will compare numerical results obtained with the isothermal and the adiabatic boundary conditions. We will observe that the results are very similar and that the choice of this boundary condition is insignificant. In practical applications, an isothermal boundary condition is considered as a good approximation, given the thermal conductivities of the wall materials.

On the sides and the axis of the domain, a free-slip boundary condition is enforced with an adiabatic condition:

$$\boldsymbol{u}' \cdot \boldsymbol{n} = 0 \ , \quad \nabla T' \cdot \boldsymbol{n} = 0 \text{ on } \Gamma_{\text{axis}} \text{ and } \Gamma_{\text{s}} \ . \tag{14}$$

This free-slip condition is indeed representative of the interaction between perforations for a normal plane wave, due to the symmetry of the configuration.

The reflection coefficient R on the surface of the perforated plate is defined by

$$R = \left(\frac{\overline{p}}{W} - \mathrm{e}^{\mathrm{i}kL_T}\right) \mathrm{e}^{\mathrm{i}kL_T}, \tag{15}$$

where $W = 1$ and $\overline{p}$ is the averaged pressure over the boundary Γ_{in}.

Thus, the normalized impedance at the surface of the perforated plate is determined using the following expression:

$$\frac{Z}{\rho_0 c_0} = \frac{R+1}{R-1}. \tag{16}$$

B. Helmholtz equation with losses model

Inside the computational domain we solve the Helmholtz equation written for pressure:

$$\nabla^2 p + \omega^2 p = 0 \text{ in } \Omega. \tag{17}$$

As for the LNSE, an incident plane wave is defined on the upper boundary of the domain by writing

$$\nabla p \cdot \boldsymbol{n} + \mathrm{i}\omega p = 2W\mathrm{i}\mathrm{e}^{+\mathrm{i}\omega L_Z} \text{ on } \Gamma_{\text{in}}. \tag{18}$$

On the axis and the sides of the domain we impose a free-slip boundary condition:

$$\nabla p \cdot \boldsymbol{n} = 0 \text{ on } \Gamma_{\text{axis}} \text{ and } \Gamma_{\text{s}}. \tag{19}$$

Even though a lossless Helmholtz equation is used in the computational domain, it is still possible to account for some visco-thermal losses through the use of a boundary condition that accounts for these effects within the acoustic boundary layers over the solid surfaces. This approach was first proposed and developed by Morse and Ingard (1968) and was recently further refined by Berggren *et al.* (2018). These equivalent boundary conditions are derived by performing an asymptotic expansion with respect to the viscous boundary layer thickness. The boundary condition derived by Berggren *et al.* (2018) reads

$$\nabla p \cdot \boldsymbol{n} = \delta_V \frac{\mathrm{i}-1}{2} \nabla_T^2 p + \delta_T \omega^2 \frac{(\gamma-1)(\mathrm{i}-1)}{2} p \text{ on } \Gamma_{\text{neck}} \text{ and } \Gamma_{\text{bc}}, \tag{20}$$

in which ∇_T^2 is the tangential Laplacian defined as

$$\nabla^2 p = \nabla_T^2 p + \frac{\partial^2 p}{\partial n^2} + (\nabla_T \cdot \boldsymbol{n}) \frac{\partial p}{\partial n}. \tag{21}$$

The dimensionless viscous and thermal boundary layer thicknesses are defined as follows

$$\delta_V = \frac{1}{Sh} \text{ and } \delta_T = \frac{1}{Sh\sqrt{Pr}}.$$

One objective of the present paper is to assess the applicability of this equivalent boundary condition to predict the acoustic impedance of perforated plate liners. Equation (20) is derived from the linearized compressible Navier–Stokes equations. A no-slip condition and an isothermal condition are applied on the rigid walls. The radius of curvature of the surface should also be large compared to the viscous boundary layer thickness. Therefore, in the case of a perforate plate, this boundary condition is valid when the radius of the neck is much larger than δ_V and δ_T. This limitation is stated by Mbailassem *et al.* (2019) in a similar approach. Since the wall model (20) is not suitable for strongly curved surfaces, this model is not expected to be valid at the corners of the hole. The corners of the perforation and their sharpness can play an important role in the acoustic dissipation, as discussed by Morse and Ingard (1968). Another limitation is that the viscous boundary layer should not interact. For a perforate plate, this occurs when $\delta_V \geq R_{\text{neck}}$. Berggren *et al.* (2018) compared their solutions to those of Keefe (1984) for cylindrical wave guides of radius 0.1 mm and obtained good correspondence for $Sh > 2$. In order to perform consistent comparisons between the numerical models and measurements, we will not consider $Sh < 2$ in the following.

Equation (20) is derived using an isothermal boundary condition. If an adiabatic boundary condition is used instead, the term $\delta_T \omega^2 (\gamma - 1)(\mathrm{i} - 1)p/2$ in (20) is removed because it represents the heat flux through the thermal boundary layer.

This model based on the classical Helmholtz equation and the equivalent boundary condition (20) allows to perform rapid predictions of the acoustic impedance of a perforated plate. This is because it involves only a single variables, compared to the LNSE which involve density, velocity and temperature. In addition, the LNSE modeled requires a very fine mesh to resolve the thermal and viscous boundary layers while the net effect of the acoustic boundary layers are directly model by the equivalent boundary condition (20). This is especially true for high frequencies, when the boundary layers are very thin. The Helmholtz with losses model is implemented using GetFEM, but other implementations could be considered. This is the case in Kampinga and Wijnant (2011) in which a similar formulation, implemented in COMSOL, based on a reduced set of the full linearized Navier-Stokes equations is proposed, to obtain a more efficient FEM model for visco-thermal acoustics.

III. NUMERICAL METHOD

The LNSE model and the Helmholtz model are both solved using the finite element method. The variational formulations are detailed in B and C. These formulations are implemented using the GetFEM++ package (Renard and Pommier, 2017) and the meshes are generated using Gmsh (Geuzaine and Remacle, 2009). Unstructured, triangular meshes are used. In the LNSE model, first order polynomials are used to approximate the density and

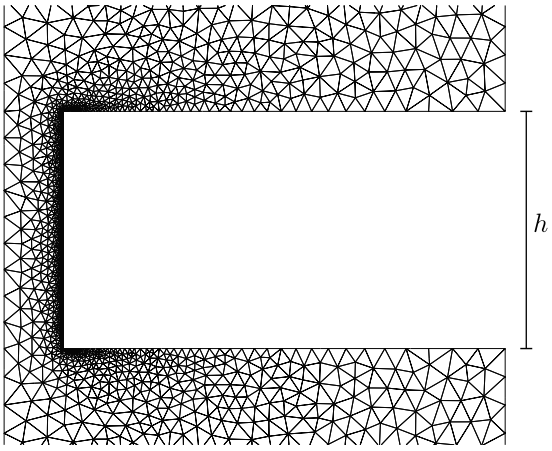

FIG. 2. Example of finite element mesh for the LNSE model.

the temperature while second-order polynomials are used for the velocity. In the Helmholtz model, the pressure field is approximated with second-order polynomials.

Figure 2 shows an example of finite element mesh used for the LNSE model. This mesh corresponds to configuration 3, detailed in Table I further below. The mesh is refined near the neck to properly resolve the boundary layers. In addition, the corners of the neck are rounded with a radius $R_c = R_{neck}/100$ to avoid geometrical singularities. No measurable difference is observed on the predicted impedance when the computations are performed using sharp corners, but rounded corners lead to a faster mesh convergence of the numerical model. This method is also used by Temiz *et al.* (2015) to perform numerical simulations based on the linearized incompressible Navier-Stokes equations.

IV. COMPARISONS WITH MEASUREMENTS

The results obtained from the numerical models are now compared with impedance tube measurements. These measurements are carried out in accordance with the NF EN ISO

Configuration	σ (%)	R_{neck} (mm)	R_{cav} (mm)	h (mm)
1 (macro)	6	0.8	3.27	1.5
2 (macro)	10	0.8	2.53	1.5
3 (micro)	1.4	0.15	1.27	0.6
4 (micro)	4.2	0.15	0.73	0.6

TABLE I. Perforated plate configurations.

10534-2 standard method. The diameter of the tube is 29 mm. The cut-on frequency of the first non plane mode is 6932 Hz. Two 1/4" microphones with a 20 mm spacing are used to determine the surface impedance of the liners. The distance between the sample and the closest microphone is 45.2 mm. The comparison between the calculation and the measurements is carried out between 850 Hz and 3000 Hz. The cavity depth is $L = 29$ mm. Four configurations are treated in this study to investigate the impact of the liner's geometry on the impedance. The chosen parameters are summarized in Table I.

Mechanical drilling is used to manufacture the perforated plates. Figure 3 shows a photography of a perforated plate cut to assess qualitatively the sharpness of the corners. We can observe that the perforations have a clear cylindrical shape and that the corners appear to be sharp. The diameter of the perforations is known within ± 0.01 mm, which provides a good accuracy on the overall porosity of the plate. In the macro-perforated case, the max-

FIG. 3. Cross-sectional view of a perforated plate with $R_{\text{neck}} = 0.9\,\text{mm}$. Note that this view does not intersect with both of the perforations axes.

imum relative error on the porosity is 1.3 % while for the micro-perforated case it is 6.8 %. More details on the accuracy of this manufacturing process can be found in Drevon (2004).

Configuration 1 and 2 correspond to macro-perforated plates with a low and high porosity respectively. Configuration 3 and 4 are micro-perforated plates with a low and high porosity. The neck radius is kept constant in the macro- and micro-perforated cases. The Sound Pressure Level (SPL) is set to 115 dB at the plate surface with a white noise source. We introduce the Strouhal number

$$St = \frac{2\omega R_{\text{neck}}}{|u_p|} \tag{22}$$

in which $|u_p|$ is the acoustic velocity through one perforation. In order to remain in the linear regime, St must be larger than 1 according to Temiz *et al.* (2016). Since we are using a white noise source, this velocity $|u_p|$ can be defined in two ways. Firstly, we can consider that the perforation is submitted to the acoustic velocity associated with each frequency independently. Secondly, we can use the root mean square velocity calculated over the complete frequency range. This is defined as follows

$$u_p = \sqrt{\sum_i u_{p,i}^2} \tag{23}$$

in which $u_{p,i}$ is the acoustic velocity at each frequency. It is necessary to check that $St > 1$ using both definitions of the velocity $|u_p|$. Figure 4 shows the Strouhal number based the

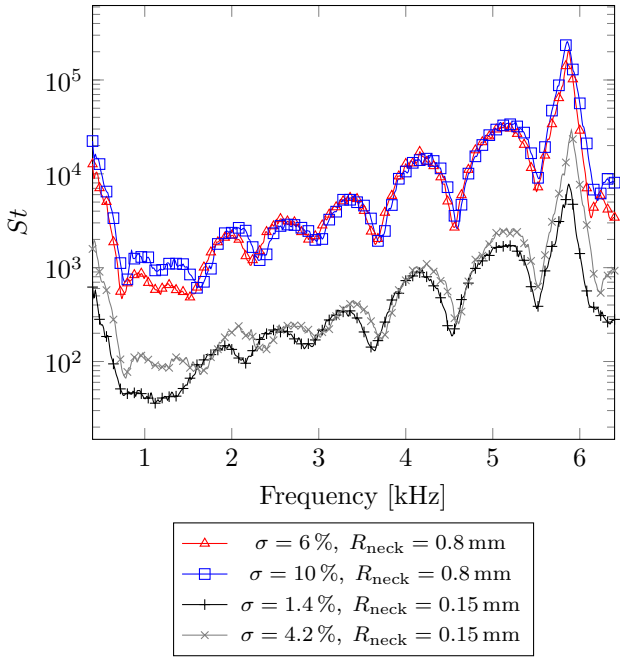

FIG. 4. (Color online) Strouhal number calculated for the 4 configurations.

acoustic velocity at each frequency. The lowest value observed between 850 Hz and 3000 Hz is $St = 36$ for configuration 3. When using the root mean square velocity calculated between 400 Hz and 6400 Hz, we see that its lowest value is $St = 2.9$.

In the following the normalized resistance $\text{Re}(Z)/(\rho_0 c_0)$ and the normalized plate reactance $\text{Im}(Z)/(\rho_0 c_0) + \cot(k_0 L)$, with $k_0 = \omega/c_0$, are plotted as functions of the shear number.

Figures 5 shows the impedances obtained for the macro-perforated plates, for which $10.6 < Sh < 20$ approximately. The LNS model appears to underestimate the resistance of the macro-perforated liners. It is also the case for the Helmholtz model but to a lesser extent. However, the significance of these differences is limited since we are looking at low

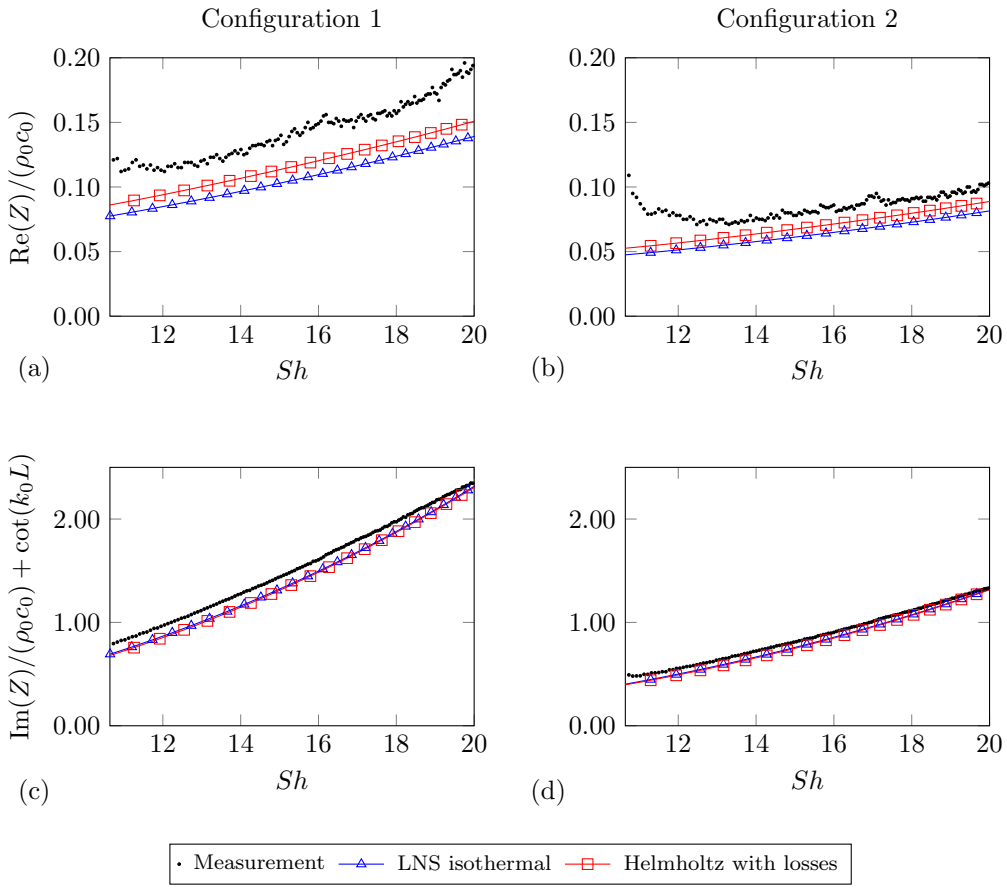

FIG. 5. (Color online) (a), (c) Normalized resistance and normalized plate reactance for configuration 1: a macro perforated case with a low porosity ($Re_a = 18201$). (b), (d) Normalized resistance and normalized plate reactance for configuration 2: a macro perforated case with a high porosity ($Re_a = 18201$).

resistance values. As a result, the corresponding absolute error is low. The computed plate reactances present a good correspondence with the measurements.

Figure 6 shows the impedances for the micro perforated configurations, for which $2 < Sh < 3.7$, which corresponds to the validity limit of the Helmholtz model. In the micro perforated case, according to Figures 6(a) and 6(b), the resistance is accurately predicted by the linearized Navier–Stokes model. The Helmholtz model also provides correct predictions

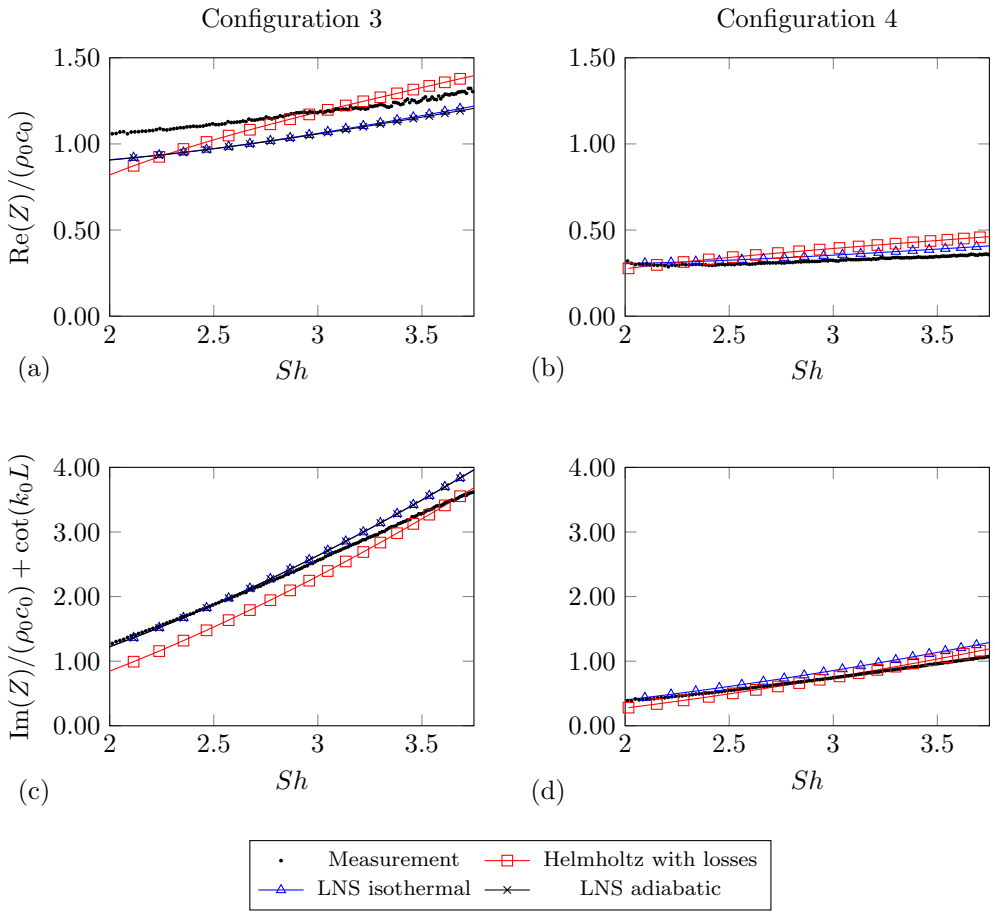

FIG. 6. (Color online) (a), (c) Normalized resistance and normalized plate reactance for configuration 3: a micro perforated case with a low porosity ($Re_a = 3413$). (b), (d) Normalized resistance and normalized plate reactance for configuration 4: a micro perforated case with a high porosity ($Re_a = 3413$).

of the resistance despite the fact that it is less accurate close to its validity limit (Figure 6(a)), *i.e.* when $Sh \simeq 2$. Good correspondence between the measured and the modelled plate reactances is visible in Figures 6(c) and 6(d).

As mentioned in the previous section, the LNSE predictions are based on the isothermal condition on the plate and the backing plate. It is interesting to assess whether the use of

an adiabatic condition would significantly change these predictions. This is shown in Figure 6(a) where the results with an adiabatic and isothermal conditions are presented side-by-side for configuration 3. Changing the nature of the thermal boundary condition only has a very limited influence on the predicted impedance. This is expected because the dissipation is dominated by shear effects rather than thermal effects in this particular case.

V. ANALYSIS OF THE RATE OF DISSIPATION

In order to gain more insight into the dissipation mechanisms influencing the impedance of a perforated plate, we calculate the viscous dissipation rate (Lighthill, 1978). From equation (6), we derive its expression, separating the dissipation due to shear and bulk effects. The dissipation rate per unit mass resulting from shear stresses is

$$\Phi_{\text{shear}} = \frac{1}{Re_a}\left\{\frac{1}{2}\left[\nabla \boldsymbol{u} + (\nabla \boldsymbol{u})^{\mathrm{T}}\right] : \left[\nabla \boldsymbol{u} + (\nabla \boldsymbol{u})^{\mathrm{T}}\right] - \frac{2}{3}\left(\nabla \cdot \boldsymbol{u}\right)^2\right\}, \tag{24}$$

and the dissipation rate per unit mass due to the bulk viscosity is:

$$\Phi_{\text{bulk}} = \frac{1}{Re_a}\mu_B \left(\nabla \cdot \boldsymbol{u}\right)^2 \ . \tag{25}$$

The expression of Φ_{shear} and Φ_{bulk} are consistent with Batchelor (1967). In the results presented below, the integral over the whole FEM domain of the dissipation due to bulk effect Φ_{bulk} was found to be negligible compared to the overall value of Φ_{shear} for all four configurations. Indeed, the dissipation due to dilatation is expected to be negligible in our range of shear number, *i.e.* $2 < Sh < 20$. For this reason, Φ_{bulk} is not discussed further.

The dissipation rates Φ_{shear} for the macro perforated configurations 1 & 2 and the micro-perforated configurations 3 & 4 are shown on Figure 7 at their respective resonance frequen-

cies for $rL^*_{\text{ref}} \in [0; R_{\text{cav}}]$ and $zL^*_{\text{ref}} \in [L - 2R_{\text{neck}}; L + h + 2R_{\text{neck}}]$. In both cases, an important part of the dissipation is localized in the neck. This well-known dissipation mechanism is modelled by the theory from Zwikker and Kosten (1949). In the case of a micro-perforated plate, the viscous boundary layer thickness is large compared to the neck radius, thus the dissipation is spread across the neck. In the macro-perforated configuration, for which the ratio Sh is high, the dissipation is concentrated close to the wall of the neck.

In addition to the viscous losses in the neck, significant losses can also be seen just outside of the neck and at its corners. However the relative magnitude of these losses varies markedly between the macro- and micro-perforated cases. In the first case, the losses are localised mainly at the corners of the neck, while in the second case they are found outside the neck, at its entrances. The net effects on the acoustic impedance of the viscous losses occuring outside the neck are generally modelled using end correction terms. For instance, Guess (1975) introduces a corrected length $h' = h + 2R_{\text{neck}}$ determined empirically. More recently, it has been possible to use numerical simulations to calculate these end correction terms more systematically. For instance, Temiz *et al.* (2015) solved the linearised incompressible Navier-Stokes equations to determine the end correction for a wide range of perforates ($1 < Sh < 35$) covering both micro- and macro-perforates. While the determination of an end correction is useful to build a simple formula for the acoustic impedance, the detailed analysis of the dissipation rate presented here helps to understand where the viscous losses are located.

In order to quantitatively assess the differences in the distribution of dissipation rate between the micro- and macro-perforated cases, the dissipation rate due to shear effects is

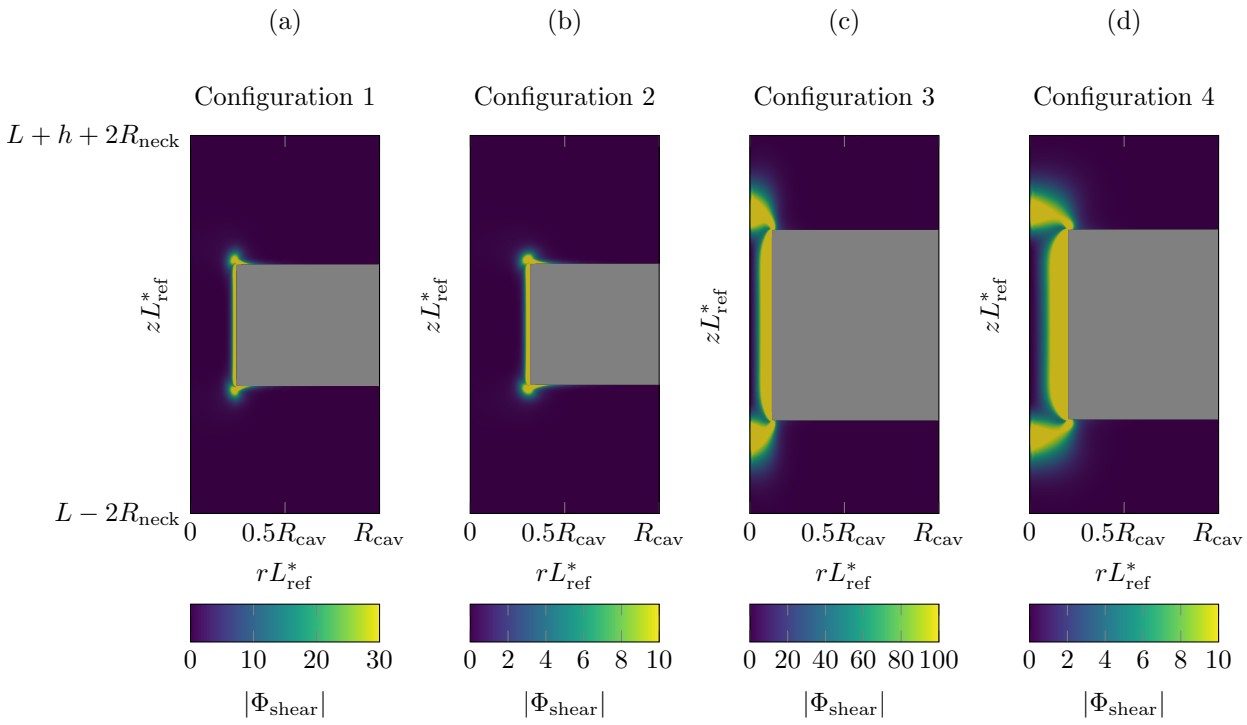

FIG. 7. (Color online) Absolute value of the dissipation rate per unit mass due to shear effects at the resonance frequency of configuration 1 at $Sh = 13.4$ (a), configuration 2 at $Sh = 15$ (b), configuration 3 at $Sh = 2.2$ (c) and configuration 4 at $Sh = 2.9$ (d).

integrated over four domains shown in Figure 8. The domains correspond to: the exterior close to the hole entrances, the neck, the wall of the neck and the corners of the neck. The contributions from these zones are computed for the four previous configurations and compared to each others.

Table II summarizes the contributions from each zone to the overall dissipation rate for each configuration at their respective resonance frequencies. The remaining losses in the domain do not exceed 0.6% for each configuration.

The relative distribution of losses is significantly different between the macro-perforated cases 1 & 2 and the micro-perforated cases 3 & 4. In the first cases, the viscous boundary

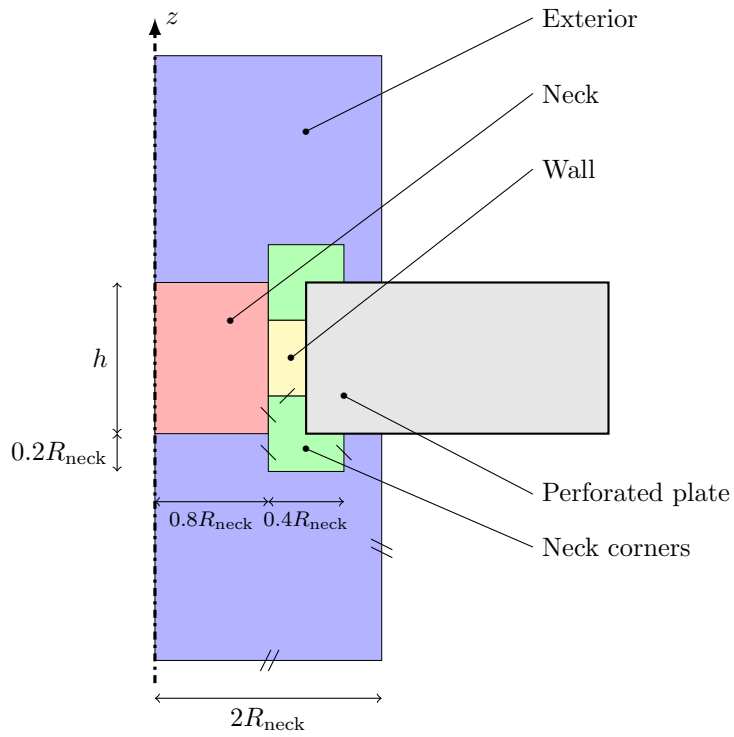

FIG. 8. (Color online) Schematic of the integrated surfaces.

layer thickness is small compared to the neck radius and the dissipation is localized mainly near the corners and along the neck wall. The important contribution from the corners is partly due to the fact that the ratio $h/(2R_{\text{neck}})$ is close to 1 in the macro perforated case, meaning that the corner integration zone extends far in the wall of the neck. Therefore, most of the losses occur close to the wall. This explains why, for macro-perforated configurations, the Helmholtz model with the equivalent boundary condition (20) is able to provide results similar to the LNSE model. In the micro-perforated cases, the shear number Sh is low and a significant contribution from the neck and the wall regions is visible. In addition, about a quarter of the losses occurs in the exterior domain, near the entrance of the holes. This highlights the presence of a jet in the linear regime when considering micro perforation.

Configuration	Sh	**Exterior** (%)	**Neck corners** (%)	**Neck** (%)	**Wall** (%)
1 (macro)	13.4	12.7	37.8	2.1	46.9
2 (macro)	15	11.1	39.4	1.6	47.5
3 (micro)	2.2	25.1	7.1	31.3	36.1
4 (micro)	2.9	25.3	7.1	31.3	36.9

TABLE II. Comparison of the contributions for each configuration.

Despite the fact that the Helmholtz approach is not modeling this effect, it so happens that, for this configuration, it provides correct predictions of the impedance.

VI. CONVERGENCE OF THE NUMERICAL MODELS

The convergence of the numerical models is investigated in this section. In a first stage, we compare the results obtained from impedance tube measurements to computations performed with different numbers of degrees of freedom (DOF) using the macro-perforated configuration 1.

Good convergence of the LNSE model is obtained with 36.8 kDOF (Figure 9(b)). This corresponds to elements of size $3.34\delta_V$ on the axis and $0.43\delta_V$ on the surface of the neck. The size of the elements on the edges of the perforation is the same as the size of the elements on the surface of the neck. In fact, the normalized plate reactance in Figure 9(d) has already converged for a very coarse model with just 11.4 kDOF. Figures 9(a) and (c) show that

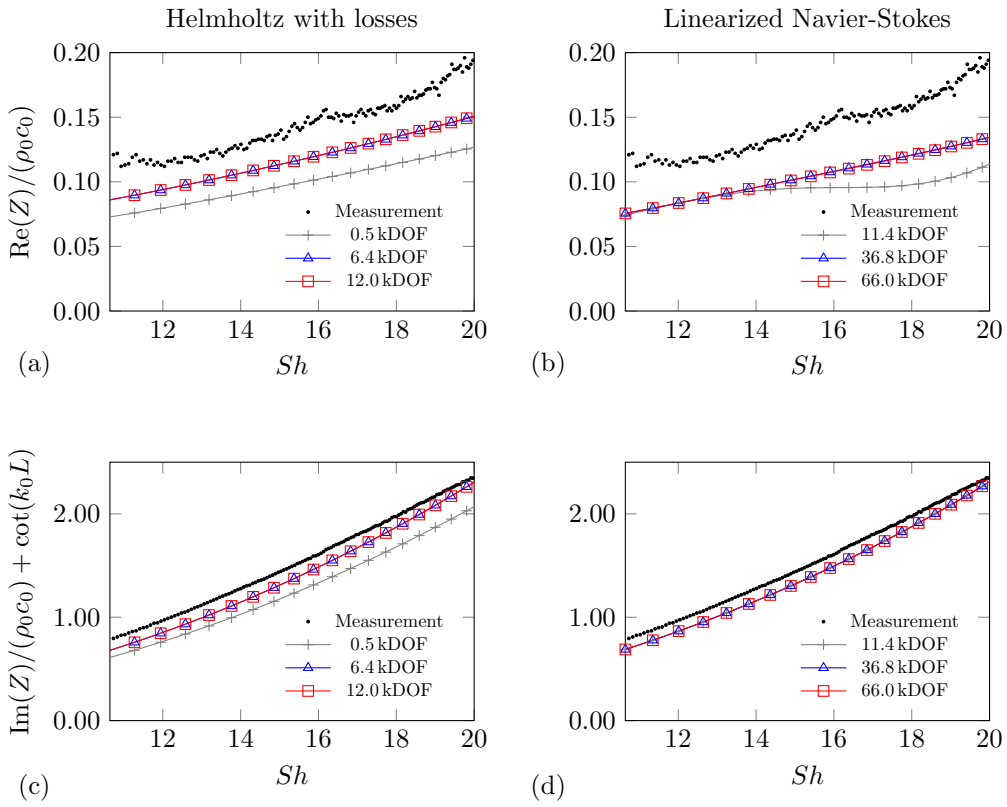

FIG. 9. (Color online) (a), (c) Measured normalized resistance and normalized plate reactance compared with the Helmholtz model for different numbers of DOF. (b), (d) Measured normalized resistance and normalized plate reactance compared with the LNSE model for different numbers of DOF.

the Helmholtz model converges for a number of DOF near 6.4 kDOF. This corresponds to elements of size $8.16\delta_V$ on the axis and $1.07\delta_V$ on the surface of the neck. This much smaller model size is explained by the facts that (i) the Helmholtz equation is a scalar model while the LNSE involves 4 variables, and (ii) there is no need to resolve the boundary layers with the Helmholtz model.

In a second stage, the accuracy of the models is investigated by computing the impedance at the resonance frequency of configuration 1. A series of computations is performed with

increasingly finer meshes. To assess the accuracy of each of these computations, the error on the predicted impedance is calculated as follows

$$\epsilon_r = \frac{|Z - Z_f|}{\rho_0 c_0}, \tag{26}$$

where Z_f is the reference value of impedance calculated for each model using an extremely fine mesh. This error on the impedance is shown in Figure 10 for configuration 1 at the resonance frequency. It is clear that the Helmholtz model with the boundary condition (20) converges more rapidly than the LNSE model. As a consequence, a converged prediction of the impedance ($\epsilon_r \simeq 10^{-4}$) is obtained with a much smaller problem size with the Helmholtz model (around 5000 degrees of freedom, compared to around 10^5 degrees of freedom for the LNSE model). This provides quantitative evidence of the computational benefits of this Helmholtz model.

VII. CONCLUSION

Two computational models were considered to predict the acoustic impedance of perforated plates in the linear regime. Both macro- and micro-perforated configurations were considered and detailed comparisons with measured data from an impedance tube were used for validation.

The model based on the linearized Navier–Stokes equations is particularly expensive to solve, but it provides a more detailed and complete picture of the absorption mechanisms. It was used to calculate the viscous dissipation rate for a single hole. It was observed that the overall distribution of dissipation is very different between the macro- and micro-

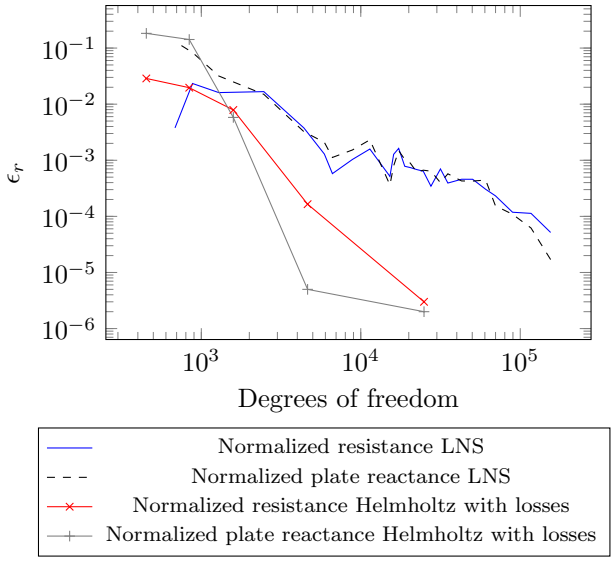

FIG. 10. (Color online) Absolute value of the difference between the the normalized impedance obtained for several grid and the finest grid. ($Re_a = 18201$).

perforated cases. For the macro-perforated case, there is a significant amount of dissipation taking place at the corners of the perforation. In the micro-perforated case, an important contribution to the viscous dissipation comes from the regions just above and below the neck. These contributions to the acoustic absorption are generally accounted by introducing end correction terms that have been determined emperically (Guess, 1975) or numerically (Temiz *et al.*, 2015). The quantitative analysis of the dissipation rate presented here provide more detailed insight into the location and significance of these dissipation mechanisms.

The second model considered is based on the classical Helmholtz equation combined with an equivalent boundary condition developed by Berggren *et al.* (2018) that accounts for the visco-thermal losses in the acoustic thermal and viscous boundary layers. This model is

much cheaper to solve compared to the LNSE since it is a scalar model and does not require to resolve the thermal and viscous boundary layers in the finite element mesh.

Based on comparisons with experimental data, both models are able to predict accurately the impedance. Despite its inherent simplifications (compared to the LNSE model), the approach based on the Helmholtz equation and the equivalent boundary condition appears to provide reliable predictions both for macro- and micro-perforated plates. While this can be expected for macro-perforates since most of the losses occur along the walls of the perforation, this is more unexpected for micro-perforates since the underlying assumption of the equivalent boundary condition are not strictly satisfied. This is however consistent with the recent results on the use of this model for predicting losses occuring in porous materials .

VIII. ACKNOWLEDGEMENT

The authors gratefully acknowledge the support from ANR Chaire industrielle MACIA (ANR-16-CHIN-0002).

APPENDIX A:

On the upper boundary Γ_{in} of the computation domain, an incoming plane wave of the form $\mathrm{e}^{+\mathrm{i}\omega t+\mathrm{i}kz}$ is generated by using the following Robin boundary condition:

$$\nabla p' \cdot \boldsymbol{n} + \mathrm{i}kp' = 2\mathrm{i}kW\mathrm{e}^{\mathrm{i}kL_Z} \text{ on } \Gamma_{in}, \tag{A1}$$

where $L_Z = L + h + L_T$ and W is the amplitude of the plane wave. The numerical implementation is formulated using the acoustic Reynolds number based on the sound speed Re_a instead of the shear number Sh which is used for the post-processing of the results. The wavenumber k remains to be determined together with the associated expression for the other variables of the linearized Navier–Stokes equations. To that end we use the fact that these variables are also of the form $\mathrm{e}^{+\mathrm{i}\omega t - \mathrm{i}kz}$ to modify equations (8), (9) and (10) and write:

$$\rho' = -\frac{k}{\omega}\boldsymbol{u}'\cdot\boldsymbol{n}\ , \quad p' = -\frac{\alpha}{k}\boldsymbol{u}'\cdot\boldsymbol{n}\ , \quad T' = -\frac{k}{\beta}\boldsymbol{u}'\cdot\boldsymbol{n}\ , \quad p' = [(\gamma-1)T' + \rho']/\gamma\ , \tag{A2}$$

with

$$\alpha = \omega - \frac{\mathrm{i}k^2}{Re_a}\left(\mu_B + \tfrac{4}{3}\right)\ , \quad \beta = \omega - \mathrm{i}k^2\frac{\gamma}{Re_a Pr}\ .$$

From these relations, and assuming that thermal effects are small, one can recover the definition of the wavenumber (12) of the dispersion relation. One can also obtain the boundary conditions for the linearized Navier–Stokes equations corresponding to an incoming plane wave:

$$\nabla\rho'\cdot\boldsymbol{n} + \mathrm{i}k\rho' = \frac{2k^3}{\omega\alpha}\mathrm{i}W\mathrm{e}^{\mathrm{i}kL_Z}\ , \tag{A3}$$

$$\nabla\left(\boldsymbol{u}'\cdot\boldsymbol{n}\right)\cdot\boldsymbol{n} + \mathrm{i}k\boldsymbol{u}'\cdot\boldsymbol{n} = \frac{-2k^2}{\alpha}\mathrm{i}W\mathrm{e}^{\mathrm{i}kL_Z}\ , \tag{A4}$$

$$\nabla T'\cdot\boldsymbol{n} + \mathrm{i}kT' = \frac{2k^3}{\alpha\beta}\mathrm{i}W\mathrm{e}^{\mathrm{i}kL_Z}\ . \tag{A5}$$

These expressions are used below in the variational formulation of the LNSE.

APPENDIX B:

1. Mass equation

The weak formulation of the mass conservation equation is

$$\int_\Omega q\frac{\partial \rho'}{\partial t}\,\mathrm{d}\Omega = \int_\Omega \boldsymbol{u}'\cdot\nabla q\,\mathrm{d}\Omega - \int_\Gamma q\boldsymbol{u}'\cdot\boldsymbol{n}\,\mathrm{d}\Gamma\,, \tag{B1}$$

where q is a test function. Incorporating the plane-wave boundary condition (A4) in equation (B1) yields

$$\int_\Omega q\frac{\partial \rho'}{\partial t}\,\mathrm{d}\Omega = \int_\Omega \boldsymbol{u}'\cdot\nabla q\,\mathrm{d}\Omega + \frac{1}{\mathrm{i}k}\int_{\Gamma_{\mathrm{in}}} q(\boldsymbol{n}\cdot\nabla)(\boldsymbol{u}'\cdot\boldsymbol{n})\,\mathrm{d}\Gamma + \frac{2k}{\alpha}W\mathrm{e}^{\mathrm{i}kL_Z}\int_{\Gamma_{\mathrm{in}}} q\,\mathrm{d}\Gamma\,. \tag{B2}$$

2. Momentum equation

The boundary including the axis and the free-slip boundaries is written $\Gamma_s = \Gamma_{\mathrm{axis}} \cup \Gamma_{\mathrm{ext,lat}} \cup \Gamma_{\mathrm{cav,lat}}$. The weak formulation of the momentum equation reads

$$\begin{aligned}\int_\Omega \boldsymbol{v}\cdot\frac{\partial \boldsymbol{u}}{\partial t}\,\mathrm{d}\Omega = {}& \frac{1}{\gamma}\int_\Omega (\nabla\cdot\boldsymbol{v})\left[(\gamma-1)T'+\rho'\right]\mathrm{d}\Omega \\ & - \frac{1}{Re_a}\int_\Omega \nabla\boldsymbol{v} : \left[\nabla\boldsymbol{u}' + (\nabla\boldsymbol{u}')^{\mathrm{T}}\right] + \left(\mu_B - \tfrac{2}{3}\right)(\nabla\cdot\boldsymbol{v})(\nabla\cdot\boldsymbol{u}')\,\mathrm{d}\Omega \\ & - \frac{1}{\gamma}\int_\Gamma (\boldsymbol{v}\cdot\boldsymbol{n})\left[(\gamma-1)T'+\rho'\right]\mathrm{d}\Gamma \\ & + \frac{1}{Re_a}\int_\Gamma \boldsymbol{v}\cdot\left[\nabla\boldsymbol{u}' + (\nabla\boldsymbol{u}')^{\mathrm{T}}\right]\boldsymbol{n} + \left(\mu_B - \tfrac{2}{3}\right)\boldsymbol{v}\cdot\boldsymbol{n}\,(\nabla\cdot\boldsymbol{u}')\,\mathrm{d}\Gamma\end{aligned} \tag{B3}$$

where $\boldsymbol{v}$ is a test function. Using the boundary conditions (A3) to (A5), we find

$$\begin{aligned}\rho_0 \int_\Omega \boldsymbol{v} \cdot \frac{\partial \boldsymbol{u}}{\partial t}\,\mathrm{d}\Omega = &\frac{1}{\gamma}\int_\Omega (\nabla\cdot\boldsymbol{v})\left[(\gamma-1)T' + \rho'\right]\mathrm{d}\Omega \\ &- \frac{1}{Re_a}\int_\Omega \nabla\boldsymbol{v} : \left[\nabla\boldsymbol{u}' + (\nabla\boldsymbol{u}')^{\mathrm{T}}\right] + \left(\mu_B - \tfrac{2}{3}\right)(\nabla\cdot\boldsymbol{v})(\nabla\cdot\boldsymbol{u}')\,\mathrm{d}\Omega \\ &+ \frac{1}{\mathrm{i}\gamma k}\int_{\Gamma_{\mathrm{in}}} (\boldsymbol{v}\cdot\boldsymbol{n})(\boldsymbol{n}\cdot\nabla)\left[(\gamma-1)T' + \rho'\right]\mathrm{d}\Gamma \\ &- \left[2We^{ikL_Z} - \frac{2Wik^2e^{ikL_Z}}{\alpha}\left(\frac{\mu_B + \frac{4}{3}}{Re_a}\right)\right]\int_{\Gamma_{in}} \boldsymbol{v}\cdot\boldsymbol{n}\,\mathrm{d}\Gamma \\ &- \frac{ik}{Re_a}\left(\mu_B + \tfrac{4}{3}\right)\int_{\Gamma_{\mathrm{in}}} (\boldsymbol{v}\cdot\boldsymbol{n})(\boldsymbol{u}'\cdot\boldsymbol{n})\,\mathrm{d}\Gamma\,.\end{aligned} \tag{B4}$$

3. Energy equation

The weak formulation of the energy equation corresponds to

$$\int_\Omega \epsilon\frac{\partial T'}{\partial t}\,\mathrm{d}\Omega = -\int_\Omega (\nabla\cdot\boldsymbol{u}')\,\epsilon - \frac{\gamma}{Re_aPr}\nabla\epsilon\cdot\nabla T'\,\mathrm{d}\Omega + \frac{\gamma}{Re_aPr}\int_\Gamma \epsilon\nabla T'\cdot\boldsymbol{n}\,\mathrm{d}\Gamma\,,$$

where ϵ is a test function. Replacing $\nabla T'\cdot\boldsymbol{n}$ by the plane-wave boundary condition (A5) on Γ_{in}, the weak formulation become

$$\begin{aligned}\int_\Omega \epsilon\frac{\partial T'}{\partial t}\,\mathrm{d}\Omega = &-\int_\Omega (\nabla\cdot\boldsymbol{u}')\,\epsilon - \frac{\gamma}{Re_aPr}\nabla\epsilon\cdot\nabla T'\,\mathrm{d}\Omega \\ &- \mathrm{i}k\frac{\gamma}{Re_aPr}\int_{\Gamma_{\mathrm{in}}}\epsilon T'\,\mathrm{d}\Gamma \\ &+ \frac{2W\mathrm{i}k^3\mathrm{e}^{\mathrm{i}kL_Z}}{\alpha\beta}\frac{\gamma}{Re_aPr}\int_{\Gamma_{\mathrm{in}}}\epsilon\,\mathrm{d}\Gamma.\end{aligned} \tag{B5}$$

APPENDIX C:

The variational formulation for the Helmholtz equation is as follows:

$$-\int_\Omega \nabla p\cdot\nabla\eta\,\mathrm{d}\Omega + \int_\Gamma \nabla p\cdot\boldsymbol{n}\eta\,\mathrm{d}\Gamma + \omega^2\int_\Omega p\eta\,\mathrm{d}\Omega = 0, \tag{C1}$$

where η is a test function.

An incoming plane wave is implemented on the upper boundary of the domain:

$$\frac{\partial p}{\partial n} + \mathrm{i}\omega p = 2W\mathrm{i}\mathrm{e}^{\mathrm{i}\omega L_Z} \text{ on } \Gamma_{\text{in}} \,. \tag{C2}$$

The boundary condition (20) is implemented on Γ_w.

These boundary conditions are introduced in (C1) to give

$$\int_\Omega -\nabla p \cdot \nabla \eta + \omega^2 p\eta \,\mathrm{d}\Omega + \int_{\Gamma_w} -\delta_V \frac{\mathrm{i}-1}{2} \nabla_T p \cdot \nabla_T \eta - \delta_T \omega^2 \frac{(\mathrm{i}-1)\,(\gamma-1)}{2} p\eta \,\mathrm{d}\Gamma_w \tag{C3}$$
$$+ \int_{\Gamma_{\text{in}}} -\mathrm{i}\omega p\eta + 2\mathrm{i}\omega \mathrm{e}^{\mathrm{i}\omega L_Z} \eta \,\mathrm{d}\Gamma_{\text{in}} = 0.$$

Batchelor, G. K. (**1967**). *An introduction to fluid dynamics* (Cambridge University Press), 151–156.

Berggren, M., Bernland, A., and Noreland, D. (**2018**). "Acoustic boundary layers as boundary conditions," Journal of Computational Physics **371**, 633–650.

Drevon, E. (**2004**). "Measurement Methods and Devices Applied to A380 Nacelle Double Degree-Of-Freedom Acoustic Liner Development," in *10th AIAA/CEAS Aeroacoustics Conference*, American Institute of Aeronautics and Astronautics, Manchester, Great Britain.

Geuzaine, C., and Remacle, J.-F. (**2009**). "Gmsh: a three-dimensional finite element mesh generator with built-in pre- and post-processing facilities," International Journal for Numerical Methods in Engineering **79**(11), 1309–1331.

Guess, A. W. (**1975**). "Calculation of perforated plate liner parameters from specified acoustic resistance and reactance," Journal of Sound and Vibration **40(1)**, 119–137.

Honzík, P., Durand, S., Joly, N., and Bruneau, M. (**2013**). "On the Acoustic Transfer Function of Slowly Tapered Small Horns Filled With Thermo-Viscous Fluid," Acta Acustica united with Acustica **99**(5), 694–702.

Ingard, U. (**1953**). "On the Theory and Design of Acoustic Resonators," The Journal of the Acoustical Society of America **25**(6), 1037–1061.

Joly, N., Bruneau, M., and Bossart, R. (**2006**). "Coupled Equations for Particle Velocity and Temperature Variation as the Fundamental Formulation of Linear Acoustics in Thermo-Viscous Fluids at Rest," Acta Acustica united with Acustica **92**, 8.

Kampinga, W. R., and Wijnant, Y. H. (**2010**). "Performance of Several Viscothermal Acoustic Finite Elements," ACTA ACUSTICA UNITED WITH ACUSTICA **96**, 10.

Kampinga, W. R., and Wijnant, Y. H. (**2011**). "An Efficient Finite Element Model for Viscothermal Acoustics," ACTA ACUSTICA UNITED WITH ACUSTICA **97**, 14.

Keefe, D. H. (**1984**). "Acoustical wave propagation in cylindrical ducts: Transmission line parameter approximations for isothermal and nonisothermal boundary conditions," The Journal of the Acoustical Society of America **75**(1), 58–62.

Laurens, S., Tordeux, S., Bendali, A., Fares, M., and Kotiuga, P. (**2013**). "Lower and upper bounds for the Rayleigh conductivity of a perforated plate," ESAIM: Mathematical Modelling and Numerical Analysis **47**(6), 1691–1712.

Lighthill, J. (**1978**). *Waves in Fluids* (Cambridge University Press), 76–85.

425 Maa, D.-Y. (**1998**). "Potential of microperforated panel absorber," The Journal of the
426 Acoustical Society of America.

427 Malinen, M., Lyly, M., Raback, P., Karkainen, A., and Karkkainen, L. (**2004**). "A Finite
428 element Method for the modeling of thermo-viscous effects in acoustics," Jyvaskyla, Fin-
429 land.

430 Mbailassem, F., Gourdon, E., Leclre, Q., Redon, E., and Cambonie, T. (**2019**). "Sound ab-
431 sorption prediction of linear damped acoustic resonators using a lightweight hybrid model,"
432 Applied Acoustics **150**, 14–26.

433 Morse, P. M., and Ingard, K. U. (**1968**). *Theoretical Acoustics* (McGraw-Hill Book Company,
434 New York), 285–300, 480–489.

435 Pryor, R. W. (**2009**). *Multiphysics modeling using COMSOL®: a first principles approach.*
436 (Jones & Bartlett Publishers).

437 Renard, Y., and Pommier, J. (**2017**). "GetFEM++. An Open Source Finite Element Li-
438 brary,".

439 Roberts, D. (**1977**). "Equivalent sand-grain roughness of perforated plate acoustic linings,"
440 in *15th Aerospace Sciences Meeting*, American Institute of Aeronautics and Astronautics,
441 Los Angeles, CA, USA.

442 Schlichting, H. (**1979**). *Boundary layer theory*, 7 ed. (McGraw-Hill Book Company).

443 Temiz, M. A., Lopez Arteaga, I., Efraimsson, G., bom, M., and Hirschberg, A. (**2015**). "The
444 influence of edge geometry on end-correction coefficients in micro perforated plates," The
445 Journal of the Acoustical Society of America **138**(6), 3668–3677.

Temiz, M. A., Tournadre, J., Arteaga, I. L., and Hirschberg, A. (**2016**). "Non-linear acoustic transfer impedance of micro-perforated plates with circular orifices," Journal of Sound and Vibration **366**, 418–428.

Zwikker, C., and Kosten, C. W. (**1949**). *Sound absorbing materials* (Elsevier, New York).